Letter

Second-harmonic generation in the topological multifold semimetal RhSi

Baozhu Lu,[1] Sharareh Sayyad,[2,3] Miguel Ángel Sánchez-Martínez,[2] Kaustuv Manna,[4,5] Claudia Felser,[4] Adolfo G. Grushin,[2,*] and Darius H. Torchinsky[1,†]

[1]*Department of Physics, Temple University, Philadelphia, Pennsylvania 19122, USA*
[2]*Univ. Grenoble Alpes, CNRS, Grenoble INP, Institut Néel, 38000 Grenoble, France*
[3]*Max Planck Institute for the Science of Light, Staudtstraße 2, 91058 Erlangen, Germany*
[4]*Max Planck Institute for Chemical Physics of Solids, Dresden D-01187, Germany*
[5]*Department of Physics, Indian Institute of Technology Delhi, New Delhi 110016, India*

(Received 18 February 2021; revised 14 May 2021; accepted 8 April 2022; published 26 April 2022)

Recent experiments in the topological Weyl semimetal TaAs have observed record-breaking second-harmonic generation (SHG), a nonlinear optical response at 2ω generated by an incoming light source at ω. However, whether SHG is enhanced in topological semimetals in general is a challenging open question because their band structure entangles the contributions arising from trivial bands and topological band crossings. In this work, we circumvent this problem by studying RhSi, a chiral topological semimetal with a simple band structure with topological multifold fermions close to the Fermi energy. We measure SHG in a wide frequency window, $\omega \in [0.27, 1.5]$ eV and, using first-principles calculations, we establish that, due to their linear dispersion, the contribution of multifold fermions to SHG is subdominant as compared with other regions in the Brillouin zone. Our calculations suggest that parts of the bands where the dispersion is relatively flat contribute significantly to SHG. As a whole, our results suggest avenues to enhance SHG responses.

DOI: 10.1103/PhysRevResearch.4.L022022

I. INTRODUCTION

Second-harmonic generation (SHG) is a nonlinear optical response that is useful in interrogating quantum phases of matter; since it only occurs in media without inversion symmetry, it is used as a proxy for spontaneous symmetry breaking [1–6] and in studies of the surface and interfacial properties of materials [7–12]. It is also widely applied technologically as the basis for generating light sources at different wavelengths [13,14]. Therefore finding systems without inversion symmetry and with a high second-harmonic yield is a contemporary material science challenge.

A central challenge to finding materials with a large SHG is identifying the microscopic origin of large nonlinear optical responses. In two recent experiments [15,16], the topological semimetal TaAs [17–23] was reported to exhibit a giant SHG response at $\omega \sim 1.5$ eV (800 nm) [15], reaching a maximum yield $\sim 2 \times 10^2$ larger than the maximum response of the semiconductor GaAs at 0.7 eV incoming photon energy [16]. The $\sim$eV frequencies at which the band structure was probed, however, were far larger than the $\sim$60 meV energy scale associated with the topological degeneracies of its low-energy band structure, the Weyl nodes. Hence the existence of Weyl nodes cannot explain the enhanced response. Instead, the enhancement was attributed phenomenologically to the skewness of the polarization distribution [16], but a general microscopic origin has yet to be uncovered. Moreover, the role of topological degeneracies with linear dispersion, such as Weyl nodes, in determining SHG remains experimentally unclear mainly due to the complex band structure of TaAs when probed at large ($\sim$eV) frequencies [15,16,24].

In this work, we show experimentally, and demonstrate theoretically that transitions between linearly dispersing bands, specifically those close to topological band degeneracies, suppress rather than enhance SHG. We do so by studying the chiral topological semimetal RhSi in space group 198, which has a relatively simple band structure [25–28] as compared with TaAs [18,29]. Close to the Fermi energy (E_F) three and four bands meet at the Brillouin center and corner, respectively, resulting in two topological degenerate points known as multifold nodes [30–33,33]. Additionally, the cubic symmetry and the absence of inversion and mirror symmetries in space group 198 simplify the analysis of SHG from RhSi because, unlike TaAs, there is only one independent component of the SHG tensor, χ^{xyz}. The simplicity of this space group has aided the interpretation of other nonlinear optical responses, notably the circular-photogalvanic effect [34–36]

We report χ^{xyz} of RhSi over a wide frequency range (see Fig. 1), i.e., from 0.27 to 1.55 eV, and compare it with first-principles calculations which, at low energies, are also benchmarked with a $k \cdot p$ model [36]. By identifying the regions in the band structure connected by optical transitions, we can infer that contributions between linearly dispersing bands are relatively small compared with those regions with relatively flat dispersion. When linear contributions are active

*adolfo.grushin@neel.cnrs.fr.
†dtorchin@temple.edu.

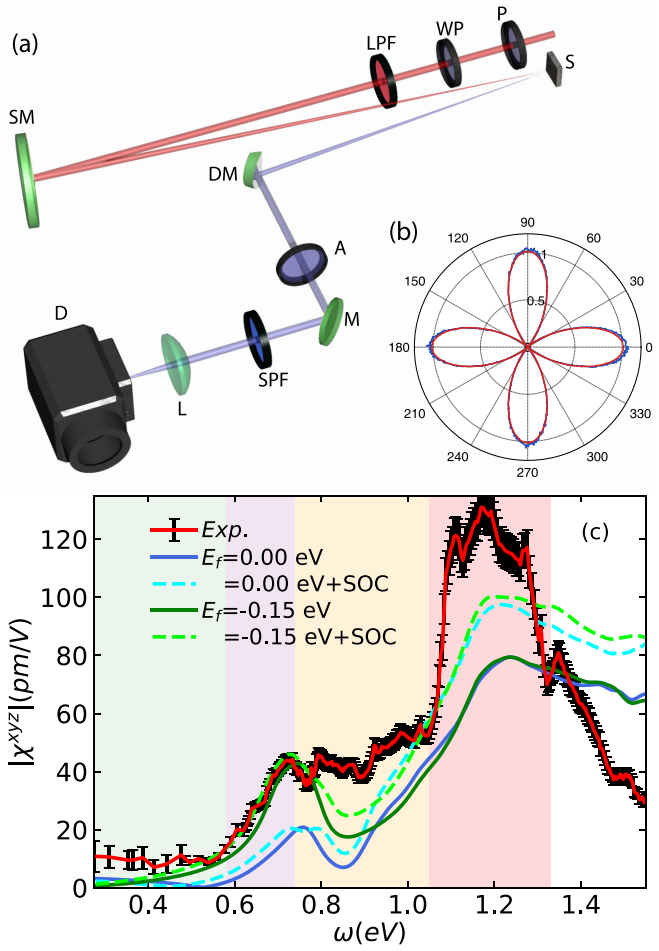

FIG. 1. (a) Schematic diagram of setup used in SHG measurements. Optics are P, polarizer; WP, waveplate; LPF, longpass filter; SM, spherical mirror; S, sample; DM, D-shaped mirror; A, analyzer; M, mirror; SPF, shortpass filter; L, lens; D, detector. (b) Representative data and fit for $\omega = 1.24$ eV. The data are in blue while the fit to Eq. (A2) in Ref. [53] is in red. (c) Experimentally measured (red line with black error bars) and theoretically calculated (colored lines) SHG susceptibilities. Fermi energies are indicated by colors $E_f = 0.0$ (blue), -0.15 (green) eV. Solid (dashed) lines present theoretical results without (with) SOC. The scissors potential is $\Delta = 1.23$ eV. Shaded areas represent the photon energies at which different transitions from the valance to conduction bands occur. See also Figs. 2(a) and 3(a) for examples of these transitions. Shaded areas span $\omega \in [0.276, 0.58]$ (green), [0.58,0.74] (purple), [0.74,1.05] (orange), and [1.05,1.33] (red) eV. For the definition of the error bars, see the Supplemental Material [53].

(green and yellow regions in Fig. 1), the increase of the SHG signal as a function of frequency is relatively small compared with other frequency regions (purple and red regions in Fig. 1). We refer to this smaller contribution as a suppression of the SHG signal. The best agreement with the data is obtained after correcting the bare separation between bands by incorporating many-body effects [37–41], suggesting that capturing other nonlinear responses in chiral topological semimetals may require these corrections as well.

At the single-particle level, the suppression of SHG from transitions involving to linear bands compared with transitions involving other types of bands can be understood from dimensional analysis [42,43]; since the SHG susceptibility χ has units of inverse energy squared (in units of fundamental constants) and the linear bands have no associated energy scale, the first finite contribution to SHG is due to quadratic corrections to the linear bands. This contribution is frequency independent because, by dimensional analysis, the SHG may scale as $1/t^2$ where t is inversely related to the band curvature. Hence linear bands, where t is large, have smaller contributions than other points in the Brillouin zone. In contrast, flatter parts of the Brillouin zone contribute with a larger density of states, resulting in a comparatively larger SHG.

RhSi crystalizes in the cubic space group $P2_13$ (number 198). Several materials in this space group, notably CoSi, RhSi, AlPt, PdGa, and PtGa [25–27,44–49], are known chiral topological semimetals that lack inversion and mirror symmetries [30–33]. Photoemission experiments revealed that these materials showed spectra consistent with a threefold degeneracy at the Γ point and a fourfold degeneracy at the zone corner [27,44–47]. These are topological band degeneracies and lead to exotic photogalvanic effects, including a quantized circular photogalvanic effect [25,50–52], which has been proven to be challenging to observe [34–36].

II. EXPERIMENT

Figure 1(a) shows a schematic diagram of our SHG setup. The output of a regeneratively amplified Ti:sapph laser producing 1.2 mJ, 35-fs pulses centered at 800 nm at a repetition rate of 5 kHz was used to pump an optical parametric amplifier (OPA) from which we derived the incoming fundamental laser field in the 800 nm–4.5 μm wavelength range ($0.276 - 1.55$ eV). More details on the experimental system can be found in the Supplemental Material [53]. The intensity of the vertically polarized SHG output was measured as a function of incoming polarization angle ϕ, an example of which is shown in Fig. 1(b) with a typical fit to the expression $2/3[\chi^{xyz}\cos(2\phi)]^2$. The fits were corrected for the experimental parameters of pulse duration, spot size, and instrument response and then normalized against a GaAs standard in order to arrive at an absolute quantitative value for the SHG susceptibility element χ^{xyz}, with results in a ratio $\chi^{xyz}_{\mathrm{GaAs}}/\chi^{xyz}_{\mathrm{RhSi}} = 2.4$ for photon energy $\omega = 1.24$ eV. This calibration procedure is described in detail in Ref. [16]. The resulting SHG in the $0.27 - 1.5$ eV energy range is shown in Fig 1(c). We note that this spectrum covers over five octaves of bandwidth and reaches, to our knowledge, a far lower energy than any SHG previously reported.

III. THEORY

We have carried out the density functional theory (DFT) calculation using the EXCITING package [54] based on state-of-the-art full-potential linearized augmented plane-wave implementations. We have employed the generalized gradient approximations within the Perdew-Burke-Ernzerhof scheme [55] as an exchange-correlation functional. The lattice parameters of the chiral cubic crystal RhSi have been chosen based on experimental measurements [25,56]. Four atoms of Rh and four atoms of Si in the unit cell are located in the Wyckoff positions for the space group $P2_13$ [27,56]. We have

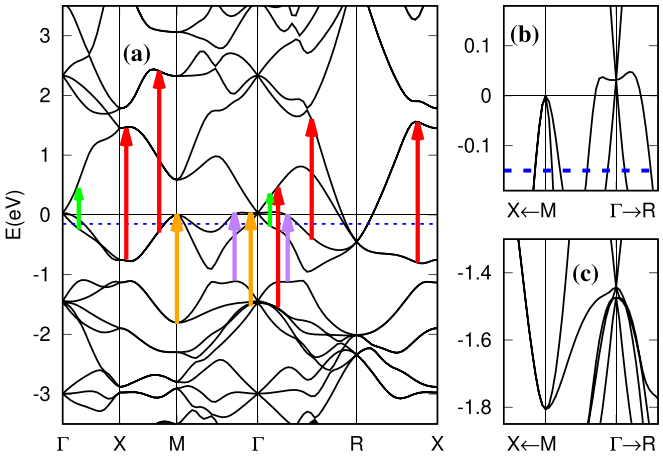

FIG. 2. (a) First-principles band structure of RhSi without SOC. Arrows indicate representative two-photon electronic transitions in SHG, and their color code corresponds to that of the shaded areas representing different frequency windows in Fig. 1(c). (b) Zoom to the low-energy bands between Γ and M points close to the Fermi level. Dashed lines indicate the Fermi energy at which the theoretical curves in Fig. 1(c) are plotted, namely, $E_f = -0.15$ (blue) eV. (c) Same as (b) but close to energy -1.6 eV. The zero of energy scale represents the Fermi energy of the pristine system.

performed our calculations on a $50 \times 50 \times 50$ k-point grid. In the following, we present our results in the presence and absence of the spin-orbit coupling (SOC).

The electronic band structure for RhSi along the lines connecting high-symmetry points in the Brillouin zone is shown in Fig. 2 when SOC is not included and in Fig. 3 in the presence of SOC. The energy is measured with respect to the Fermi energy of the pristine system $E_f = 0$ eV. Close to

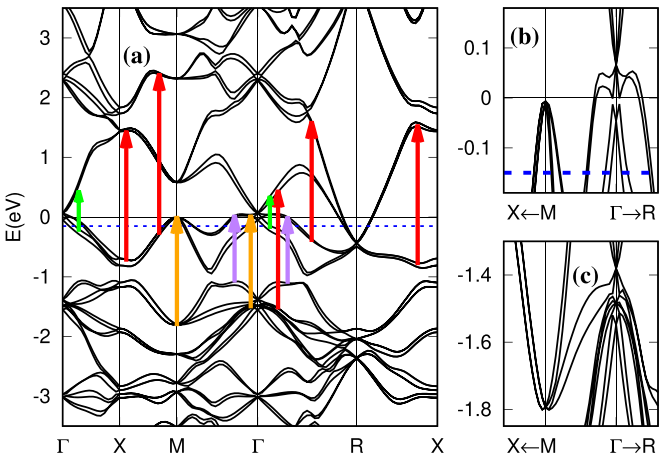

FIG. 3. (a) First-principles band structure of RhSi with SOC. Arrows indicate representative two-photon electronic transitions in SHG, and their color code corresponds to that of the shaded areas representing different frequency windows in Fig. 1(c). (b) Zoom to the low-energy bands between the Γ and M points close to the Fermi level. Dashed lines indicate the Fermi energy at which the theoretical curves in Fig. 1(c) are plotted, namely, $E_f = -0.15$ eV. (c) Same as (b) but close to energy -1.6 eV. The zero of energy scale represents the Fermi energy of the pristine system.

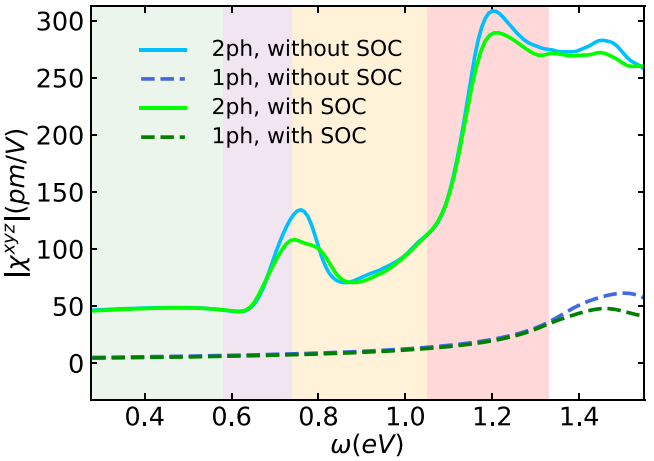

FIG. 4. Calculated different components of SHG from two-photon (solid sky blue line), one-photon (dashed royal blue line) transitions calculated without SOC as well as two-photon (solid green line), one-photon (dashed dark green line) transitions in the presence of SOC. Both sets of results are at Fermi energy $E_f = -0.15$ eV. The total SHG susceptibility is plotted in Fig. 1(c) and scissors potential $\Delta = 1.23$ eV.

the Fermi energy, the electronic structure possesses a threefold degeneracy at the Γ point, Fig. 2(b) and Fig. 3(b), and a fourfold degenerate point at the R point. We note that degenerate threefold crossings also exist at different energies at the Γ point, e.g., around $E \approx -1.57$ eV, a region magnified in Fig. 2(c) and Fig. 3(c).

Our *ab initio* results for the nonlinear susceptibility χ^{xyz} of RhSi are shown in Fig. 1(c); see Ref. [53] for more details. As in the experimental analysis, we also calibrate our results with GaAs [57]. The position of the Fermi energy in our system is determined indirectly, as in other optics experiments [35,36]. To account for the effects of disorder and finite temperature in our experimental sample, we have employed a Gaussian broadening with width $\delta = 0.1$ eV, consistent with previous findings [35]. We also include a scissors shift [39] of $\Delta = 1.23$ eV to account for renormalized occupied and unoccupied bands due to many-body effects; see Ref. [53].

Our results for RhSi, for Fermi energies that lie below the threefold node ($0.0 - 0.15$ eV) in the presence/absence of SOC, are shown in Fig. 1(c). For RhSi, we observe that for $\omega \lesssim 0.6$ eV, theory (with/without SOC) and experiment are in reasonable agreement. One should note that for $\omega < 0.4$, the agreement between theory and four data points of the experiment deteriorates in which the experimental data exhibit nearly 50% errors. This low-energy regime is, not coincidentally, where the experiment is extraordinarily challenging to perform due to both a lack of sensitive detection technology and an absence of standard candle calibrants.

The small SHG yield in the green frequency window $\omega \in [0.276, 0.58]$ in Fig. 1(c) is a result of the suppressed optical transitions between low-energy linearly dispersing bands close to the Γ point; see green arrows in Figs. 2 and 3. To support this conclusion we first separate one-photon (ω) and two-photon (2ω) transitions contributing to χ^{xyz} in Fig. 4. We observe that two-photon transitions dominate the green frequency region regardless including or excluding the SOC.

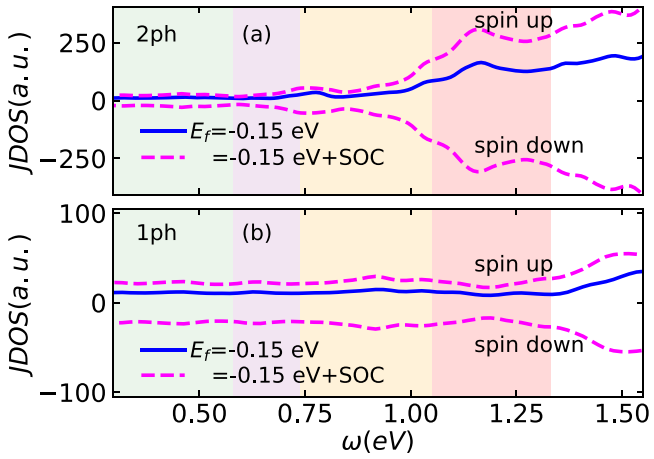

FIG. 5. Optical joint density of states for SHG from two-photon (a) and one-photon (b) contributions calculated without SOC (solid blue lines) and in the presence of SOC (dashed magenta lines). In the presence of SOC, spin-resolved JDOS is plotted. Note the different vertical scales in each panel.

Next, we compare this result to the two-photon and one-photon joint density of states (JDOS) in Figs. 5(a) and 5(b), respectively. The JDOS counts allowed optical transitions between occupied (with energy ω_n) and unoccupied (with energy ω_m) states ignoring their associated matrix elements, i.e., $\mathrm{JDOS}(\Omega) = \sum_{m,n} \delta(\omega_m - \omega_n - \Omega)$, where $\Omega = 2\omega\,(= \omega)$ for the two-(one-)photon JDOS. In the green frequency window, the one-photon JDOS dominates compared with the two-photon JDOS, cf. Figs. 5(a) and 5(b). Comparing with Fig. 4, this indicates that the optical matrix elements suppress the one-photon contribution to χ^{xyz}, reducing the overall SHG for $\omega < 0.58\,\mathrm{eV}$. The band structures in Figs. 2 and 3 suggest that the contribution to one-photon processes in this frequency region arises from linear bands around Γ, whose matrix elements therefore suppress SHG.

In order to further understand the low-energy region and to benchmark our DFT calculations, we have developed a low-energy $k \cdot p$ model; see the Supplemental Material [53]. This model captures low-energy excitations around the Γ point and brings insight into understanding the optical transitions resulting from the threefold node. Specifically, the SHG response around Γ displays a broad, low-energy peak below the experimentally accessible frequencies. This single peak results from the merging of a dominant two-photon peak with a subdominant one-photon peak due to the large $\delta \approx 100$ meV. A qualitatively similar broadened peak is also present by DFT when $\Delta = 0$, which additionally receives contributions not captured by the $k \cdot p$ model. Consequently, the DFT peak is broader compared with that found using the $k \cdot p$ model. When $\Delta \neq 0$, the DFT results show that this low-energy peak is largely suppressed. This is because Δ is a correction that pushes occupied and empty bands away from each other, and thus the optical transitions responsible for the peak are pushed to higher energies, resulting in a better agreement with the experimental data. These results highlight the fact that both the many-body corrections, modeled with a scissors potential Δ, and the quasiparticle broadening δ are essential to explain the experimental measurements.

In addition, we note that the scissors potential Δ favors two-photon contributions. The reason is that, by separating occupied and unoccupied states, Δ reduces the available phase space for one-photon transitions with $\omega < \Delta$. In contrast, the phase space for two-photon transitions is only reduced for lower photon energies, $\omega < \Delta/2$. As a result, two-photon transitions dominate for $\omega < \Delta$, as seen in Fig. 4.

We move on to analyze the purple frequency window in Fig. 1(c), i.e., $\omega \in [0.58, 0.74]\,\mathrm{eV}$. The SHG increases in this region, a feature that is well captured in our calculation when $E_f < 0\,\mathrm{eV}$ irrespective of whether SOC is included or not. Separately plotting one- and two-photon contributions as before in Fig. 4 reveals that the two-photon response in the purple energy window is dominant. Consistent with our discussion in the previous paragraph, the rise of the two-photon contributions occurs around $\omega \approx \Delta/2$ in the JDOS. When compared with the band structure, the observation of a dominant two-photon transition in Fig. 4 suggests that two partially flat bands close to the Γ point, separated by approximately 1.3 eV and connected by two-photon excitations (purple arrows) in Figs. 2 and 3, are responsible for enhancing χ^{xyz} in the purple energy window. The width of this energy window is comparable to the quasiparticle broadening ($\delta = 0.1\,\mathrm{eV}$), supporting their flat band origin.

At photon energies $\omega \in [0.74, 1.05]\,\mathrm{eV}$, i.e., in the orange window in Fig. 1(c), the data exhibit a plateaulike structure. Our DFT calculations show that this feature is reproduced better when SOC is present for $E_f = -0.15\,\mathrm{eV}$. Naively, one would expect that in this frequency window, the one-photon electronic transitions from linear bands close to the R point are activated. However, Figs. 4 and 5 reveal that the one-photon contribution (dashed lines) is small compared with the dominant two-photon transitions. The small contribution of the linearly dispersing bands close to the R point is expected by dimensional analysis and confirmed by our results. The two-photon transitions responsible for SHG in this region likely involve dispersing valance bands around the M and Γ points, as indicated by the orange arrows in Figs. 2 and 3.

Last, there is a drastic increase of χ^{xyz} measured within the red energy window of $\omega \in [1.05, 1.33]\,\mathrm{eV}$ in Fig. 1(c). Our theoretical results also report an increased SHG yield in this energy range with a sharper rise when SOC is included. Once more we can identify the substantial role of two-photon transitions compared with the smaller one-photon contribution; see Figs. 4 and 5. The large photon energies that define this energy window enable electrons to reach a considerable number of bands exemplified by red arrows in Figs. 2 and 3. As frequency increases, we observe quantitative differences between our DFT results and the experimental measurements, especially when $\omega > 1.33\,\mathrm{eV}$. These deviations could be attributed to the insufficient many-body corrections in our first-principles calculations.

IV. CONCLUSIONS

In summary, our SHG spectra on RhSi together with our first principles and $k \cdot p$ calculations show that one-photon transitions among relatively linear bands have a small contribution to SHG. Because of the linear dispersion, these transitions are suppressed compared with the dominant

two-photon transitions among other types of dispersive bands including those between relatively flat bands, account for the observed SHG signal. At the single-particle level, this result is consistent with the expectation that one-photon transitions are more likely to connect linear bands close to E_f, which are expected by dimensional analysis to suppress the SHG. An additional, many-body effect results from a sizable scissors potential Δ, which separates occupied and unoccupied states and favors two-photon over one-photon transitions. We expect that materials in the same space group such as AlPt [46], PdGa [47,49], and PtGa [48] behave similarly.

Our findings complement earlier observations that predict the enhancement of SHG due to other factors, such as the skewness of the polarization distribution [16] or a significant intersite hopping [58]. Taken together, these results outline strategies to find materials with high SHG yield.

ACKNOWLEDGMENTS

S.S. thanks G. Davino for his suggestions on improving DFT calculations. We thank F. de Juan, J. E. Moore, T. Morimoto, J. Orenstein, D. Parker, L. Wu, and Y. Zhang for discussions and related collaborations. A.G.G. and S.S. acknowledge funding by the ANR under Grant ANR-18-CE30-0001-01 (TOPODRIVE). A.G.G. is also funded by the European Union Horizon 2020 research and innovation program under Grant Agreement No. 829044 (SCHINES). M.A.S.M. is supported by the European Union's Horizon 2020 research and innovation programme under the Marie-Sklodowska-Curie Grant Agreement No. 754303 and the GreQuE Cofund programme. D.H.T. acknowledges Temple University startup funding. K.M. and C.F. acknowledge the financial support from the European Research Council (ERC) Advanced Grant No. 742068 "TOP-MAT," European Union's Horizon 2020 research and innovation program (Grants No. 824123 and No. 766566), and Deutsche Forschungsgemeinschaft (DFG) through SFB 1143. K.M. acknowledges the Max Planck Society for the funding support under Max Planck-India partner group project. The work at Temple University was funded in part by the National Science Foundation under Award No. NSF/DMR-1945222.

B.L. and S.S. contributed equally.

[1] Y. R. Shen, Surface second harmonic generation: A new technique for surface studies, Annu. Rev. Mater. Sci. **16**, 69 (1986).

[2] Y. R. Shen, Surface properties probed by second-harmonic and sum-frequency generation, Nature (London) **337**, 519 (1989).

[3] A. Dähn, W. Hübner, and K. H. Bennemann, Symmetry Analysis of the Nonlinear Optical Response: Second Harmonic Generation at Surfaces of Antiferromagnets, Phys. Rev. Lett. **77**, 3929 (1996).

[4] J. C. Petersen, M. D. Caswell, J. S. Dodge, I. A. Sergienko, J. He, R. Jin, and D. Mandrus, Nonlinear optical signatures of the tensor order in $Cd_2Re_2O_7$, Nat. Phys. **2**, 605 (2006).

[5] J. W. Harter, Z. Y. Zhao, J.-Q. Yan, D. G. Mandrus, and D. Hsieh, A parity-breaking electronic nematic phase transition in the spin-orbit coupled metal Cd_2 Re_2 O_7, Science **356**, 295 (2017).

[6] N. Sirica, P. P. Orth, M. S. Scheurer, Y. M. Dai, M. C. Lee, P. Padmanabhan, L. T. Mix, S. W. Teitelbaum, M. Trigo, L. X. Zhao, G. F. Chen, B. Xu, R. Yang, B. Shen, C. C. Lee, H. Lin, T. A. Cochran, S. A. Trugman, J. X. Zhu, M. Z. Hasan *et al.*, Photocurrent-driven transient symmetry breaking in the Weyl semimetal TaAs, Nat. Mater. **21**, 62 (2022).

[7] V. Mizrahi and J. E. Sipe, Phenomenological treatment of surface second-harmonic generation, J. Opt. Soc. Am. B **5**, 660 (1988).

[8] R.-P. Pan, H. D. Wei, and Y. R. Shen, Optical second-harmonic generation from magnetized surfaces, Phys. Rev. B **39**, 1229 (1989).

[9] Y. M. Chang, L. Xu, and H. W. K. Tom, Observation of Coherent Surface Optical Phonon Oscillations by Time-Resolved Surface Second-Harmonic Generation, Phys. Rev. Lett. **78**, 4649 (1997).

[10] A. Kirilyuk and T. Rasing, Magnetization-induced-second-harmonic generation from surfaces and interfaces, J. Opt. Soc. Am. B **22**, 148 (2005).

[11] D. Hsieh, J. W. McIver, D. H. Torchinsky, D. R. Gardner, Y. S. Lee, and N. Gedik, Nonlinear Optical Probe of Tunable Surface Electrons on a Topological Insulator, Phys. Rev. Lett. **106**, 057401 (2011).

[12] C. Lee, F. Katmis, P. Jarillo-Herrero, J. S. Moodera, and N. Gedik, Direct measurement of proximity-induced magnetism at the interface between a topological insulator and a ferromagnet, Nat. Commun. **7**, 1 (2016).

[13] 2. far-infrared wave generation, in *Physical Principles of Far-Infrared Radiation*, Methods in Experimental Physics, edited by L.C. Robinson (Academic Press, 1973), Vol. 10, pp. 10–81.

[14] J. Zhao, J. Fan, W. Liu, H. Shi, N. Xiao, and M. Hu, Ultra-broadband second-harmonic generation in ZnO nano-tetrapod with over-one-octave bandwidth, IEEE Photonics Technol. Lett. **31**, 250 (2019).

[15] L. Wu, S. Patankar, T. Morimoto, N. L. Nair, E. Thewalt, A. Little, J. G. Analytis, J. E. Moore, and J. Orenstein, Giant anisotropic nonlinear optical response in transition metal monopnictide Weyl semimetals, Nat. Phys. **13**, 350 (2017).

[16] S. Patankar, L. Wu, B. Lu, M. Rai, J. D. Tran, T. Morimoto, D. E. Parker, A. G. Grushin, N. L. Nair, J. G. Analytis, J. E. Moore, J. Orenstein, and D. H. Torchinsky, Resonance-enhanced optical nonlinearity in the Weyl semimetal TaAs, Phys. Rev. B **98**, 165113 (2018).

[17] N. P. Armitage, E. J. Mele, and A. Vishwanath, Weyl and Dirac semimetals in three-dimensional solids, Rev. Mod. Phys. **90**, 015001 (2018).

[18] H. Weng, C. Fang, Z. Fang, B. A. Bernevig, and X. Dai, Weyl Semimetal Phase in Noncentrosymmetric Transition-Metal Monophosphides, Phys. Rev. X **5**, 011029 (2015).

[19] B. Q. Lv, H. M. Weng, B. B. Fu, X. P. Wang, H. Miao, J. Ma, P. Richard, X. C. Huang, L. X. Zhao, G. F. Chen, Z. Fang, X. Dai, T. Qian, and H. Ding, Experimental Discovery of Weyl Semimetal TaAs, Phys. Rev. X **5**, 031013 (2015).

[20] S.-Ming Huang, S.-Y. Xu, I. Belopolski, C.-C. Lee, G. Chang, B. Wang, N. Alidoust, G. Bian, M. Neupane, C. Zhang, S. Jia, A. Bansil, H. Lin, and M. Hasan, A Weyl fermion semimetal with surface Fermi arcs in the transition metal monopnictide TaAs class, Nat. Commun. **6**, 7373 (2015).

[21] L. X. Yang, Z. K. Liu, Y. Sun, H. Peng, H. F. Yang, T. Zhang, B. Zhou, Y. Zhang, Y. F. Guo, M. Rahn, D. Prabhakaran, Z. Hussain, S. K. Mo, C. Felser, B. Yan, and Y. L. Chen, Weyl semimetal phase in the non-centrosymmetric compound TaAs, Nat. Phys. **11**, 728 (2015).

[22] S.-Y. Xu, I. Belopolski, N. Alidoust, M. Neupane, G. Bian, C. Zhang, R. Sankar, G. Chang, Z. Yuan, C.-C. Lee *et al.*, Discovery of a Weyl fermion semimetal and topological Fermi arcs, Science **349**, 613 (2015).

[23] B. Q. Lv, N. Xu, H. M. Weng, J. Z. Ma, P. Richard, X. C. Huang, L. X. Zhao, G. F. Chen, C. E. Matt, F. Bisti *et al.*, Observation of weyl nodes in taas, Nat. Phys. **11**, 724 (2015).

[24] Z. Li, Y.-Q. Jin, T. Tohyama, T. Iitaka, J.-X. Zhang, and H. Su, Second harmonic generation in the Weyl semimetal TaAs from a quantum kinetic equation, Phys. Rev. B **97**, 085201 (2018).

[25] G. Chang, S.-Y. Xu, B. J. Wieder, D. S. Sanchez, S.-M. Huang, I. Belopolski, T.-R. Chang, S. Zhang, A. Bansil, H. Lin, and M. Z. Hasan, Unconventional Chiral Fermions and Large Topological Fermi Arcs in RhSi, Phys. Rev. Lett. **119**, 206401 (2017).

[26] P. Tang, Q. Zhou, and S.-C. Zhang, Multiple Types of Topological Fermions in Transition Metal Silicides, Phys. Rev. Lett. **119**, 206402 (2017).

[27] D. S. Sanchez, I. Belopolski, T. A. Cochran, X. Xu, J. X. Yin, G. Chang, W. Xie, K. Manna, V. Süß, C. Y. Huang, N. Alidoust, D. Multer, S. S. Zhang, N. Shumiya, X. Wang, G. Q. Wang, T. R. Chang, C. Felser, S. Y. Xu, S. Jia *et al.*, Topological chiral crystals with helicoid-arc quantum states, Nature (London) **567**, 500 (2019).

[28] T. A. Cochran, G. Chang, I. Belopolski, K. Manna, D. S. Sanchez, Z. Chéng, J.-X. Yin, H. Borrmann, J. Denlinger, C. Felser, H. Lin, and M. Zahid Hasan, A Fermi Arc Quantum Ladder, arXiv:2004.11365 (2020).

[29] J. Buckeridge, D. Jevdokimovs, C. R. A. Catlow, and A. A. Sokol, Bulk electronic, elastic, structural, and dielectric properties of the Weyl semimetal TaAs, Phys. Rev. B **93**, 125205 (2016).

[30] J. L. Mañes, Existence of bulk chiral fermions and crystal symmetry, Phys. Rev. B **85**, 155118 (2012).

[31] B. J. Wieder, Y. Kim, A. M. Rappe, and C. L. Kane, Double Dirac Semimetals in Three Dimensions, Phys. Rev. Lett. **116**, 186402 (2016).

[32] B. Bradlyn, J. Cano, Z. Wang, M. G. Vergniory, C. Felser, R. J. Cava, and B. A. Bernevig, Beyond Dirac and Weyl fermions: Unconventional quasiparticles in conventional crystals, Science **353**, aaf5037 (2016).

[33] G. Chang, B. J. Wieder, F. Schindler, D. S. Sanchez, I. Belopolski, S.-M. Huang, B. Singh, D. Wu, T.-R. Chang, T. Neupert *et al.*, Topological quantum properties of chiral crystals, Nat. Mater. **17**, 978 (2018).

[34] D. Rees, K. Manna, B. Lu, T. Morimoto, H. Borrmann, C. Felser, J. E. Moore, D. H. Torchinsky, and J. Orenstein, Helicity-dependent photocurrents in the chiral Weyl semimetal RhSi, Sci. Adv. **6**, eaba0509 (2020).

[35] Z. Ni, B. Xu, M.-Á. Sánchez-Martínez, Y. Zhang, K. Manna, C. Bernhard, J. W. F. Venderbos, F. de Juan, C. Felser, A. G. Grushin, and L. Wu, Linear and nonlinear optical responses in the chiral multifold semimetal RhSi, npj Quantum Mater. **5**, 96(2020).

[36] Z. Ni, K. Wang, Y. Zhang, O. Pozo, B. Xu, X. Han, K. Manna, J. Paglione, C. Felser, A. G. Grushin *et al.*, Giant topological longitudinal circular photo-galvanic effect in the chiral multifold semimetal CoSi, Nat. Commun. **12** (2021).

[37] Z. H. Levine and D. C. Allan, Linear Optical Response in Silicon and Germanium Including Self-Energy Effects, Phys. Rev. Lett. **63**, 1719 (1989).

[38] J. L. P. Hughes and J. E. Sipe, Calculation of second-order optical response in semiconductors, Phys. Rev. B **53**, 10751 (1996).

[39] F. Nastos, B. Olejnik, K. Schwarz, and J. E. Sipe, Scissors implementation within length-gauge formulations of the frequency-dependent nonlinear optical response of semiconductors, Phys. Rev. B **72**, 045223 (2005).

[40] B. Sadhukhan, Y. Zhang, R. Ray, and J. van den Brink, First-principles calculation of shift current in chalcopyrite semiconductor $ZnSnP_2$, Phys. Rev. Mater. **4**, 064602 (2020).

[41] W. Song, G.-Y. Guo, S. Huang, L. Yang, and L. Yang, First-principles studies of second-order nonlinear optical properties of organic-inorganic hybrid halide perovskites, Phys. Rev. Appl. **13**, 014052 (2020).

[42] X. Yang, K. Burch, and Y. Ran, Divergent bulk photovoltaic effect in Weyl semimetals, arXiv:1712.09363.

[43] O. Pozo and F. de Juan, Computing observables without eigenstates: Applications to bloch hamiltonians, Phys. Rev. B **102**, 115138 (2020).

[44] Z. Rao, H. Li, T. Zhang, S. Tian, C. Li, B. Fu, C. Tang, L. Wang, Z. Li, W. Fan *et al.*, Observation of unconventional chiral fermions with long Fermi arcs in CoSi, Nature (London) **567**, 496 (2019).

[45] D. Takane, Z. Wang, S. Souma, K. Nakayama, T. Nakamura, H. Oinuma, Y. Nakata, H. Iwasawa, C. Cacho, T. Kim, K. Horiba, H. Kumigashira, T. Takahashi, Y. Ando, and T. Sato, Observation of Chiral Fermions with a Large Topological Charge and Associated Fermi-Arc Surface States in CoSi, Phys. Rev. Lett. **122**, 076402 (2019).

[46] N. B. M. Schröter, D. Pei, M. G. Vergniory, Y. Sun, K. Manna, F. de Juan, J. A. Krieger, V. Süss, M. Schmidt, P. Dudin *et al.*, Chiral topological semimetal with multifold band crossings and long Fermi arcs, Nat. Phys.1 (2019).

[47] N. B. M. Schröter, S. Stolz, K. Manna, F. de Juan, M. G. Vergniory, J. A. Krieger, D. Pei, T. Schmitt, P. Dudin, T. K. Kim, C. Cacho, B. Bradlyn, H. Borrmann, M. Schmidt, R. Widmer, V. N. Strocov, and C. Felser, Observation and control of maximal chern numbers in a chiral topological semimetal, Science **369**, 179 (2020).

[48] M. Yao, K. Manna, Q. Yang, A. Fedorov, V. Voroshnin, B. V. Schwarze, J. Hornung, S. Chattopadhyay, Z. Sun, S. N. Guin, J. Wosnitza, H. Borrmann, C. Shekhar, N. Kumar, J. Fink, Y. Sun, and C. Felser, Observation of giant spin-split Fermi-arc with maximal Chern number in the chiral topological semimetal PtGa, Nat. Commun. **11**, 2033 (2020).

[49] P. Sessi, F.-R. Fan, F. Küster, K. Manna, N. B. M. Schröter, J.-R. Ji, S. Stolz, J. A. Krieger, D. Pei, T. K. Kim, P. Dudin, C.

Cacho, R. Widmer, H. Borrmann, W. Shi, K. Chang, Y. Sun, C. Felser, and S. S. P. Parkin, Handedness-dependent quasiparticle interference in the two enantiomers of the topological chiral semimetal PdGa, Nat. Commun. **11**, 3507 (2020).

[50] F. de Juan, A. G. Grushin, T. Morimoto, and J. E. Moore, Quantized circular photogalvanic effect in Weyl semimetals, Nat. Commun. **8**, 15995 (2017).

[51] E. J. König, H.-Y. Xie, D. A. Pesin, and A. Levchenko, Photogalvanic effect in Weyl semimetals, Phys. Rev. B **96**, 075123 (2017).

[52] F. Flicker, F. de Juan, B. Bradlyn, T. Morimoto, M. G. Vergniory, and A. G. Grushin, Chiral optical response of multifold fermions, Phys. Rev. B **98**, 155145 (2018).

[53] See Supplemental Material at http://link.aps.org/supplemental/10.1103/PhysRevResearch.4.L022022 for details on the experimental measurements, details on calculating the second-harmonic generation response function within the scissor approximation, the SHG in family of transition metal silicides, and further details on the low-energy model discussed in the main text.

[54] A. Gulans, S. Kontur, C. Meisenbichler, D. Nabok, P. Pavone, S. Rigamonti, S. Sagmeister, U. Werner, and C. Draxl, exciting: a full-potential all-electron package implementing density-functional theory and many-body perturbation theory, J. Phys.: Condens. Matter **26**, 363202 (2014).

[55] J. P. Perdew, K. Burke, and M. Ernzerhof, Generalized Gradient Approximation Made Simple, Phys. Rev. Lett. **77**, 3865 (1996).

[56] I. Engström and T. Johnsson, Least-squares refinement of the structure of RhSi (FeSi-type), Acta Chem. Scand. **19**, 1508 (1965).

[57] S. Bergfeld and W. Daum, Second-Harmonic Generation in GaAs: Experiment Versus Theoretical Predictions of $\chi^{(2)}_{xyz}$, Phys. Rev. Lett. **90**, 036801 (2003).

[58] L. Z. Tan and A. M. Rappe, Upper limit on shift current generation in extended systems, Phys. Rev. B **100**, 085102 (2019).

Supplementary Material: Suppression of second-harmonic generation from linear bands in the topological multifold semimetal RhSi

Baozhu Lu,[1,*] Sharareh Sayyad,[2,3,*] Miguel Ángel Sánchez-Martínez,[2] Kaustuv Manna,[4,5] Claudia Felser,[4] Adolfo G. Grushin,[2,†] and Darius H. Torchinsky[1,‡]

[1] *Department of Physics, Temple University, Philadelphia, PA 19122, USA*
[2] *Univ. Grenoble Alpes, CNRS, Grenoble INP, Institut Néel, 38000 Grenoble, France*
[3] *Max Planck Institute for the Science of Light, Staudtstraße 2, 91058 Erlangen, Germany*
[4] *Max Planck Institute for Chemical Physics of Solids, Dresden D-01187, Germany*
[5] *Department of Physics, Indian Institute of Technology Delhi, New Delhi 110016, India*

A. EXPERIMENTAL DETAILS

The light source was described in the main text as an optical parametric amplifier (OPA, Light Conversion - TOPAS Twins) pumped by a regeneratively amplified Ti:sapph laser system (Coherent - Astrella). The polarization of the OPA output was purified using a linear wire grid polarizer (Thorlabs - WP12L-UB) and then passed through a quarter waveplate (Thorlabs - AQWP05M-980, AQWP05M-1600 or Alphalas - PO-TWP-L4-25-FIR) matched to the photon energy to produce a circularly polarized beam. After removing parasitic wavelengths due to other nonlinear optical processes in the OPA (as well as from interactions with the optics themselves), the beam was passed through a mechanically-driven polarizer spinning at 5 Hz in order to generate a varying incoming polarization angle ϕ. For photon energies > 0.480 eV, the beam was then focused onto the sample using a 50 cm reflecting mirror at near-normal incidence so as to produce a relatively large spot. This enables high laser power to be incident on the sample while restricting the fluence to below the damage threshold. It also permitted for more SHG photons to be emitted per laser shot, yielding large enough signals to be measured by detection electronics in the IR frequency range where detector responsivity is relatively low. For photon energies < 0.480 eV, the beam instead was focused using a Cassegrain objective (Edmund Optics - 68-188) in order to obtain high enough fluences to produce measurable signals. The incidence angle introduced by the reflective objective was accounted for in the data analysis.

After reflecting from the sample, the beam was incident on a D-shaped mirror and then passed through an analyzer that was chosen to remain stationary in the vertical orientation to produce the signal $I(\phi)$. Upon emerging from the polarizer, the beam passed through a filter assembly to remove the fundamental wavelength while preserving the second-harmonic response. The filters that we used were: 2 shortpass 650 nm (Thorlabs - FESH0650) and 2 shortpass 700 nm filters for the $800-1200$ nm wavelength range; 2 shortpass 800 nm (Thorlabs - FESH0800) and 2 shortpass 1000 nm (Thorlabs - FESH0800) filters for the $1140-1500$ nm wavelength range; 2 longpass 600 nm (Thorlabs - FELH0600), 2 shortpass 900 nm (Thorlabs - FESH0900) and 2 shorpass 1000 nm (Thorlabs - FESH1000) filters for the $1400-1620$ nm wavelength range; 2 longpass 700 nm (Thorlabs - FELH0700) and 2 shortpass 1326 nm (Semrock - FF01-1326/SP-25) filters for the $1580-2000$ nm wavelength range; 2 shortpass 1326 nm (Semrock - FF01-1326/SP-25) and 2 shorpass 1550 nm (Spectrogon - SP-1550) filters for the $2000-2600$ nm wavelength range; 2 shortpass 1550 nm (Spectrogon - SP-1550) for 2800 nm; and 2 shortpass 2600 nm filters (Spectrogon - SP-2600) for the $3500-4500$ nm wavelength range.

The detectors we used were: a multialkali photocathode photomultiplier tube (Hamamatsu - R12829) biased by a high voltage power supply socket assembly (Hamamatsu - C12597-01) for incoming wavelength range $800-1620$ nm with transimpedance amplification performed by a charge sensitive preamplifier (Cremat CR-Z-PMT) in tandem with a shaping device (Cremat - CR-S-8us-US); an InGaAs photodiode (Thorlabs - FGA01) with transimpedance amplification performed by a charge sensitive preamplifier (Cremat - CR-Z-110) and a shaping device (Cremat - CR-S-8us-US) for incoming wavelength range $1580-2800$ nm; and a cooled InGaAs photodiode (Hamamatsu G12183-203K) for the $2600-4700$ nm incoming wavelength range, also attached to the same charge integrator/shaper as used for the $1580-2800$ photon range. In the $800-2800$ nm wavelength range, the intensity was recorded using a data acquisition card-based fast-sampling technique, a more detailed description of which is provided within Ref [1], whereas for the $2600-4700$ nm wavelength range, the signal was measured using a lock-in amplifier (Zurich Instruments - MFLI) locked to the laser repetition rate.

Experiments were conducted on the polished (111) face of RhSi. Further details on the sample preparation can be found in a prior publication [2]. On this face, the second-harmonic generation susceptibility tensor is given by

* These two authors contributed equally

† adolfo.grushin@neel.cnrs.fr
‡ dtorchin@temple.edu

$$\chi^{ijk}(2\omega;\omega,\omega)=\frac{1}{\sqrt{3}}\begin{pmatrix}\begin{pmatrix}0\\ \sqrt{2}\chi^{xyz}\\ -\chi^{xyz}\end{pmatrix} & \begin{pmatrix}\sqrt{2}\chi^{xyz}\\ 0\\ 0\end{pmatrix} & \begin{pmatrix}-\chi^{xyz}\\ 0\\ 0\end{pmatrix}\\ \begin{pmatrix}\sqrt{2}\chi^{xyz}\\ 0\\ 0\end{pmatrix} & \begin{pmatrix}0\\ -\sqrt{2}\chi^{xyz}\\ -\chi^{xyz}\end{pmatrix} & \begin{pmatrix}0\\ -\chi^{xyz}\\ 0\end{pmatrix}\\ \begin{pmatrix}-\chi^{xyz}\\ 0\\ 0\end{pmatrix} & \begin{pmatrix}0\\ -\chi^{xyz}\\ 0\end{pmatrix} & \begin{pmatrix}0\\ 0\\ 2\chi^{xyz}\end{pmatrix}\end{pmatrix}. \tag{A1}$$

The data were taken for incident polarization of the fundamental light dynamically rotating as angle ϕ. As detailed above, there was a static polarizer in front of the detector to measure the emitted SHG for both vertical outgoing polarization, referred to as I_{0°. Using the tensor of Eq. (1), we get

$$I(\phi)=\frac{2}{3}\left[\chi^{xyz}(2\omega;\omega,\omega)\cos(2\phi)\right]^2 \tag{A2}$$

as the expected response to which the data of Fig. 1 were fit. In order to build a spectrum, these fits were also controlled for photon-energy-dependent variable laser parameters including the incident power I_ω^2, spot size d and pulse duration τ, as well as the detector responsivity and filter transmission coefficients according to the equation

$$I_{2\omega}\propto(\chi^{\rm shg}_{ijk})^2\frac{I_\omega^2 d^2}{f^2\lambda^2\tau}. \tag{A3}$$

where $I_{2\omega}$ is the measured SHG intensity, f is the focal length of the lens, and λ is the incident wavelength. A derivation of these normalization parameters can be found in Ref. [3]. Several data points were taken in common between different detectors to account for differing detector sensitivity.

The error bars of Fig. **??**c were calculated using standard error propagation methods on Eq. 3 which requires a numerical estimate of the errors in the quantities $I_{2\omega}$, I_ω, d, and τ. The error in $I_{2\omega}$ was retrieved from the fitting routine used to obtain the fits of, e.g., Fig. **??**b, while the error in I_ω was determined from measuring the variability in the laser power at all the measured wavelengths. Error in both the spot size and pulse duration were determined from repeated measurement of these quantities.

B. SECOND-HARMONIC GENERATION RESPONSE FUNCTION WITHIN THE SCISSORS APPROXIMATION

The nonlinear polarization describing second-harmonic generation induced by an electric field $E^b(\omega)$ at a frequency ω along the Cartesian coordinate b is written in the length gauge [4] as

$$P^a(2\omega)=\chi^{abc}(2\omega;\omega,\omega)E^b(\omega)E^c(\omega), \tag{B4}$$

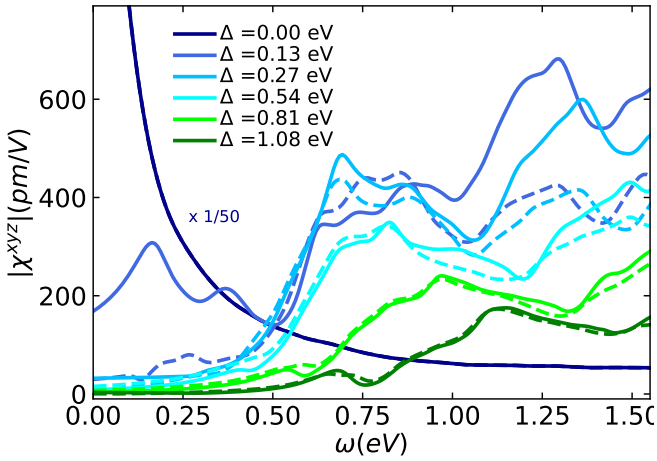

Figure S1. Different scissors corrections for χ in pristine RhSi ($E_f=0$) with a disorder broadening of $\delta=0.1$ eV. Solid (Dashed) lines present results without (with) spin-orbit coupling. Note that results with spin-orbit coupling for $\Delta=0.0$ eV are identical to results with the same Δ (solid dark blue line). For the visibility purpose, we multiplied all results with $\Delta=0.0$ eV by 1/50.

where χ^{abc} is the second-order susceptibility which satisfies the intrinsic permutation symmetry $\chi^{abc}=\chi^{acb}$.

The non-linear response function χ^{abc} accounts for interband and intraband contributions [5], and has the form

$$\begin{aligned}\chi^{abc}(2\omega;\omega,\omega)=&\chi^{abc}_{\rm 2ph}(\omega)+\chi^{abc}_{\rm 1ph}(\omega), &\text{(B5)}\\ =&\chi^{abc}_{\rm 2ph,inter}(\omega)+\chi^{abc}_{\rm 1ph,inter}(\omega)\\ &+\chi^{abc}_{\rm 2ph,intra}(\omega)+\chi^{abc}_{\rm 1ph,intra}(\omega)\\ &+\sigma^{abc}(\omega), &\text{(B6)}\end{aligned}$$

where the labels 2ph and 1ph denote two- and one-photon transitions, respectively, $\chi^{abc}_{\rm 2ph}=\chi^{abc}_{\rm 2ph,inter}+\chi^{abc}_{\rm 2ph,intra}$, and $\chi^{abc}_{\rm 1ph}=\chi^{abc}_{\rm 1ph,inter}+\chi^{abc}_{\rm 1ph,intra}+\sigma^{abc}$. The above terms of χ^{abc} are

$$\chi^{abc}_{\rm 2ph,inter}(\omega)=C\int_k\sum_{nml}\frac{r^a_{nm}\{r^b_{ml}r^c_{ln}\}}{(\omega_{ln}-\omega_{ml})}\frac{2f_{nm}}{(\omega_{mn}-2\omega)}, \tag{B7}$$

$$\chi^{abc}_{\rm 1ph,inter}(\omega) = C\int_k \sum_{nml} \frac{r^a_{nm}\{r^b_{ml}r^c_{ln}\}}{(\omega_{ln}-\omega_{ml})}\Big[\frac{f_{ml}}{\omega_{ml}-\omega}+\frac{f_{ln}}{\omega_{ln}-\omega}\Big], \tag{B8}$$

$$\chi^{abc}_{\rm 2ph,intra}(\omega) = C\int_k \sum_{nm} \frac{r^a_{nm}\{\Delta^b_{mn}r^c_{mn}\}}{\omega^2_{mn}}\frac{-8{\rm i}f_{nm}}{(\omega_{mn}-2\omega)} + C\int_k \sum_{nml} \frac{r^a_{nm}\{r^b_{ml}r^c_{ln}\}}{\omega^2_{mn}}\frac{2f_{nm}(\omega_{ml}-\omega_{ln})}{(\omega_{mn}-2\omega)}, \tag{B9}$$

$$\chi^{abc}_{\rm 1ph,intra}(\omega) = C\int_k \sum_{nml} r^a_{nm}\{r^b_{ml}r^c_{ln}\}\frac{\omega_{mn}f_{nl}}{\omega^2_{ln}(\omega_{ln}-\omega)} - C\int_k \sum_{nml} r^a_{nm}\{r^b_{ml}r^c_{ln}\}\frac{\omega_{mn}f_{ml}}{\omega^2_{ml}(\omega_{ml}-\omega)}, \tag{B10}$$

$$\sigma^{abc}(\omega) = \frac{{\rm i}C}{2}\int_k \sum_{nml} \omega_{nl}r^a_{lm}\{r^b_{mn}r^c_{nl}\}\frac{f_{nm}}{\omega^2_{mn}(\omega_{mn}-\omega)} - \frac{{\rm i}C}{2}\int_k \sum_{nml} \omega_{lm}r^a_{nl}\{r^b_{lm}r^c_{mn}\}\frac{f_{nm}}{\omega^2_{mn}(\omega_{mn}-\omega)} + \frac{{\rm i}C}{2}\int_k \sum_{nm} \frac{f_{nm}\Delta^a_{nm}\{r^b_{mn}r^c_{nm}\}}{\omega^2_{mn}(\omega_{mn}-\omega)}, \tag{B11}$$

where $C = e^3/\hbar^2$, the wave vector k is defined in the Brillouin zone, $\int_k = \int {\rm d}^3k/(4\pi^3)$, lowercase Roman subscripts denote band indices, the energy of band n is $\hbar\omega_n$, and the frequency difference is defined as $\omega_{mn} = \omega_m - \omega_n$. Here, r_{mn} are matrix elements of the position operator given by $r^a_{nm} = v^a_{nm}/({\rm i}\omega_{mn})$, and $\Delta^a_{mn} = v^a_{mm} - v^a_{nn}$, where v^a_{nm} denote the velocity matrix elements. The curly brackets impose symmetrization with respect to the Cartesian coordinates such that $\{A^a_{ml}B^b_{ln}\} = \frac{1}{2}(A^a_{ml}B^b_{ln} + B^a_{ml}A^b_{ln})$.

To evaluate the matrix elements and band energies, we have calculated the ground-state properties using the density functional theory (DFT). While these calculations can provide a satisfactory description for the occupied states, treating unoccupied states, which might be occupied during optical transitions, lacks many-body effects. As a result, the theoretical calculation of optical responses fails to exactly evaluate the energies at which the photons will be absorbed [6–8]. There are two main approaches to remedy this mismatch between theoretical and experimental results: (i) the many-body GW formalism [9–11], and (ii) the scissors approximation [4, 5, 12–14].

The GW corrections are computed using a many-body self-energy. This self-energy corrects the energy gaps between occupied and unoccupied bands and thus improves the agreement between theoretical and experimental measurements [15]. Despite these advantages, converging the well-established GW self-consistent loop is computationally demanding.

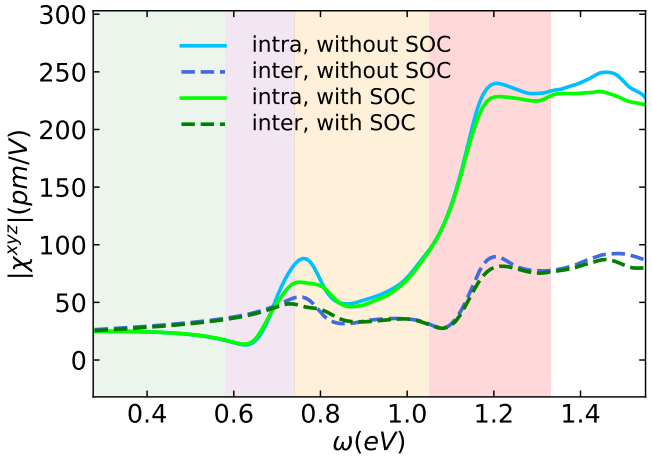

Figure S2. Intraband (solid lines) and interband (dashed lines) contributions of χ^{xyz} of RhSi in the absence (blue) and presence (green) of the spin-orbit coupling. The Fermi energy is set to $E_f = -0.15$eV. The parameters and colors of shaded areas are the same as Fig. 1(c) in the main text.

In this work we tackle the problem of inaccurate band gaps between occupied and unoccupied states using a scissors shift (Δ). Within the scissors approximation, the position and velocity matrix elements are modified as

$$r_{nm} = \frac{\tilde{v}_{nm}}{{\rm i}\big[\omega_{nm} + \frac{\Delta}{\hbar}(\delta^{\rm unoc}_n - \delta^{\rm unoc}_m)\big]}, \tag{B12}$$

$$\tilde{v}_{nm} = v_{nm}\frac{\omega_{nm} + \frac{\Delta}{\hbar}(\delta^{\rm unoc}_n - \delta^{\rm unoc}_m)}{\omega_{nm}}, \tag{B13}$$

where $\delta^{\rm unoc}_n$ is the Kronecker delta for unoccupied state n. We illustrate the influence of Δ on shifting the absorption energy in the nonlinear response χ^{xyz} in Fig. S1. The results are calculated for the pristine RhSi system ($E_f = 0$). The figure shows that by adjusting the energy gaps with Δ, optical transitions can be modified.

C. INTRABAND AND INTERBAND CONTRIBUTIONS IN SECOND-HARMONIC GENERATION OF RHSI

The intraband and interband contributions accounted in χ^{xyz} read

$$\chi^{xyz}_{\rm intra}(\omega) = \chi^{xyz}_{\rm 2ph,intra}(\omega) + \chi^{xyz}_{\rm 1ph,intra}(\omega), \tag{C14}$$

$$\chi^{xyz}_{\rm inter}(\omega) = \chi^{xyz}_{\rm 2ph,inter}(\omega) + \chi^{xyz}_{\rm 1ph,inter}(\omega), \tag{C15}$$

where $\chi^{xyz}_{\rm 2ph,inter}$, $\chi^{xyz}_{\rm 1ph,inter}$, $\chi^{xyz}_{\rm 2ph,intra}$, and $\chi^{xyz}_{\rm 1ph,intra}$ are given by Eqs. (7, 8, 9, 10), respectively. Fig. S2 presents $\chi^{xyz}_{\rm intra}$ and $\chi^{xyz}_{\rm inter}$ for RhSi with $E_f = -0.15$ eV, see also Fig. 1(c) for the total SHG yield. For $\omega \lesssim 0.9$ eV the interband and intraband contributions exhibit comparable responses in the green, purple, and orange energy windows. Combined with the observation that two-photon

transitions are dominant in RhSi, e.g., see Fig. 4 in the main text, the leading components responsible for χ^{xyz} in these regions are $\chi^{xyz}_{\text{2ph,inter}}$ and $\chi^{xyz}_{\text{2ph,intra}}$. For $\omega \in [1.05, 1.33]$ eV, the intraband contributions dominate compared with interband responses, and thus in this region the two-photon intraband transitions are responsible for the observed nonlinear SHG response.

D. LOW-ENERGY SINGLE-PARTICLE SECOND-HARMONIC GENERATION IN RHSI: $k \cdot p$ MODEL

To study the SHG at low energies near the Γ point (shaded green region in Fig. 1) we use a three-band $k \cdot p$ model with up-to-second order terms in momentum. This model was originally presented in Ref. [16] for CoSi, a material that crystallizes in the same space group (SG198) as RhSi. Here we give an overview of the construction of this model and the relevance of the different terms. For a more detailed explanation on the symmetries involved we refer the reader to Ref. [16].

It is illustrative to start by considering a higher-symmetry point group, O, to later on break the symmetry down to T, the physical point group at Γ, by including the necessary terms.

We will work the Gell-Mann matrices λ_α which form a basis for the operators acting on the subspace of the three basis states for the threefold crossing at Γ

$$\lambda_0 = \mathbb{1}, \quad \lambda_1 = \begin{pmatrix} 0 & -\mathrm{i} & 0 \\ \mathrm{i} & 0 & 0 \\ 0 & 0 & 0 \end{pmatrix}, \quad \lambda_2 = \begin{pmatrix} 0 & 0 & -\mathrm{i} \\ 0 & 0 & 0 \\ \mathrm{i} & 0 & 0 \end{pmatrix}, \tag{D16}$$

$$\lambda_3 = \begin{pmatrix} 0 & 0 & 0 \\ 0 & 0 & -\mathrm{i} \\ 0 & \mathrm{i} & 0 \end{pmatrix}, \quad \lambda_4 = \begin{pmatrix} 0 & 1 & 0 \\ 1 & 0 & 0 \\ 0 & 0 & 0 \end{pmatrix}, \tag{D17}$$

$$\lambda_5 = \begin{pmatrix} 0 & 0 & 1 \\ 0 & 0 & 0 \\ 1 & 0 & 0 \end{pmatrix}, \quad \lambda_6 = \begin{pmatrix} 0 & 0 & 0 \\ 0 & 0 & 1 \\ 0 & 1 & 0 \end{pmatrix}, \tag{D18}$$

$$\lambda_7 = \begin{pmatrix} 1 & 0 & 0 \\ 0 & -1 & 0 \\ 0 & 0 & 0 \end{pmatrix}, \quad \lambda_8 = \begin{pmatrix} \frac{1}{\sqrt{3}} & 0 & 0 \\ 0 & \frac{1}{\sqrt{3}} & 0 \\ 0 & 0 & -\frac{2}{\sqrt{3}} \end{pmatrix}. \tag{D19}$$

The point group O is generated by C_2 rotations around (110), C_2 rotations around (100), and C_3 rotations around (111). This allows four different combinations of the Gell-Mann matrices that transform as the irreducible representations (irreps) of O,

$$A_1 = \lambda_0, \tag{D20}$$

$$T_1 = (-\lambda_2, \lambda_5, -\lambda_7), \tag{D21}$$

$$T_2 = (\lambda_1, \lambda_4, \lambda_6), \tag{D22}$$

$$E = (-\frac{1}{2}\lambda_3 + \frac{\sqrt{3}}{2}\lambda_8, -\frac{\sqrt{3}}{2}\lambda_3, -\frac{1}{2}\lambda_8), \tag{D23}$$

where A_1, T_1, T_2, E label the different irreps considered. We find for the same point group O four momentum irreps up to second order in momentum,

$$K_{A_1} = k_x^2 + k_y^2 + k_z^2, \tag{D24}$$

$$K_{T_1} = (k_x, k_y, k_z), \tag{D25}$$

$$K_{T_2} = (k_y k_z, k_x k_z, k_x k_y), \tag{D26}$$

$$K_E = (k_x^2 - k_y^2, (2k_z^2 - k_x^2 - k_y^2)/\sqrt{3}). \tag{D27}$$

We can now build the most general symmetry-allowed Hamiltonian up to second order with point group symmetry O by making scalar combinations of the momentum irreps with the Gell-Mann matrices, which reads

$$H_O = \begin{pmatrix} ak^2 + \frac{2c}{3}(k^2 - 3k_z^2) & \mathrm{i}vk_x + bk_y k_z & -\mathrm{i}vk_y + bk_x k_z \\ -\mathrm{i}vk_x + bk_y k_z & ak^2 + \frac{2c}{3}(k^2 - 3k_y^2) & \mathrm{i}vk_z + bk_x k_y \\ \mathrm{i}vk_y + bk_x k_z & -\mathrm{i}vk_z + bk_x k_y & ak^2 + \frac{2c}{3}(k^2 - 3k_x^2) \end{pmatrix}, \tag{D28}$$

where $k = \sqrt{k_x^2 + k_y^2 + k_z^2}$, and a, v_F, b, and c are the parameters corresponding to the terms coming from A_1, T_1, T_2, and E, respectively.

Finally, we need to consider the point group T, obtained by breaking the C_2 rotations around (100) in the point group O. This leads to a new momentum irrep $K_E^{'} = (-(2k_z^2 - k_x^2 - k_y^2)/\sqrt{3}, k_x^2 - k_y^2)$, allowing for a new term in the $k \cdot p$ Hamiltonian, which reads

$$H_T = H_O + \frac{2d}{\sqrt{3}} \begin{pmatrix} k_y^2 - k_x^2 & 0 & 0 \\ 0 & k_x^2 - k_z^2 & 0 \\ 0 & 0 & k_z^2 - k_y^2 \end{pmatrix}. \tag{D29}$$

In previous calculations using this model (c.f. Ref [16]) the effect of d proved to be negligible in other optical responses like the circular photo-galvanic effect. Nevertheless, in this work, it is crucial to include the symmetry breaking term with a finite d parameter since the SHG response is forbidden for the point group O, but generically finite for the point group T [16, 17].

The eigenvectors and eigenvalues of the $k \cdot p$ model do not depend on d up to second order in k [16, 17], and thus we cannot use their analytical expressions to fit the value of d. To obtain the low-energy model parameters, we fit the existing four-band tight-binding model constructed for space group 198 [18, 19] to the DFT bands shown in Fig. **??**, and obtain the $k \cdot p$ parameters by fitting the $k \cdot p$ model to the tight-binding model. The resulting values for the parameters are $(a, b, c, d, v_F) = (-0.0438344, -0.01, 0.131377, 0.1874, 0.385)$. These parameters set the threefold node at $E = 0$. Finally,

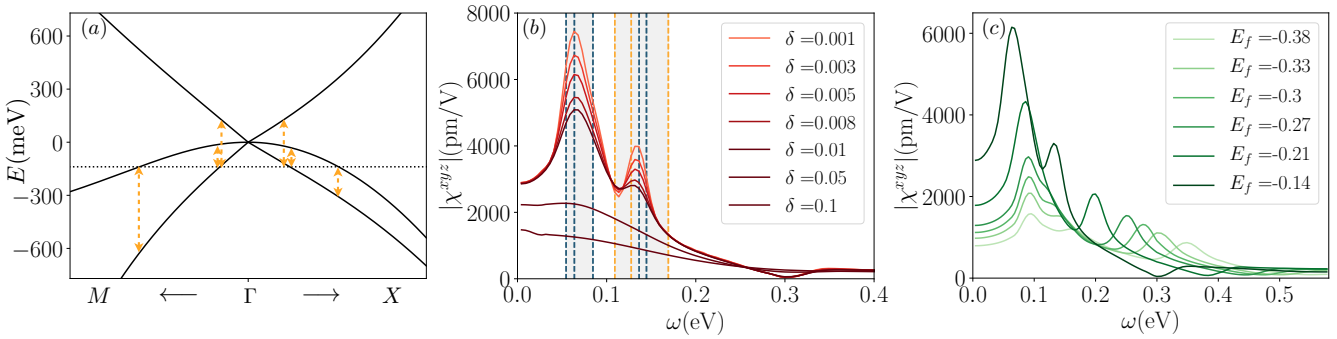

Figure S3. (a) Band structure of the $k \cdot p$ model along the $\Gamma \to X$ and $\Gamma \to M$ directions with parameters $(a, b, c, d, v_F) = (-0.0438344, -0.01, 0.131377, 0.1874, 0.385)$. The threefold node is placed at $E_\Gamma = 0$ eV, and the Fermi level is placed at $E_f = -0.14$ eV. The vertical dashed arrows indicate the most relevant one-photon activation energies. (b) Nonlinear susceptibility (solid lines) of the $k \cdot p$ model shown in (a) for different values of disorder δ. The energy regions where the most relevant transitions are activated are indicated in shaded grey. The vertical dashed lines indicate the two-photon activation frequencies (blue) and the one-photon activation frequencies (ocher). (c) Nonlinear susceptibility for different values of E_f shown in different shades of green with a disorder $\delta = 0.005$ eV.

to test the different values of E_f and compare with the DFT calculation we add a term to the Hamiltonian $H = H_T - E_f \mathbb{1}_{3\times3}$.

The nonlinear susceptibility of the $k \cdot p$ model features a two-peak structure at low energies. The energy regions where these peaks appear are delimited by the activation frequencies of the transitions from the lowest to the middle band and from the lowest to the upper band (see Fig. S3(a)). The first peak is dominated by the two-photon transitions from the lowest to the middle band (see Fig. S3(b), vertical dashed blue lines and shaded grey region). The lower, second peak in Fig. S3(b) appears in the energy region (shaded gray) delimited by one-photon transitions from the lower to the middle band (vertical ocher lines) and the two-photon transitions from the middle to the upper band (vertical blue lines).

As the disorder broadening δ is increased, the features of the nonlinear response are smoothed, and the two-peak structure is no longer distinguishable at $\delta = 0.05$ eV (Fig. S3(b)) for $E_f = 0.14$ eV. For higher δ, the nonlinear response features a single, wider and smoother peak, similar to the one obtained in the DFT calculation with $\Delta = 0$ eV (see Fig. S1 (a), dark blue curve).

The activation frequencies, and thus the position and width of the peaks, depend on the Fermi level. As the threefold node at Γ is separated from the Fermi level, the activation frequencies and the difference between them become larger. As a result, the peak positions are shifted towards higher energies. The peaks also become wider, because the energy regions delimited by the activation frequencies are spread over a larger range of energies (see Fig. S3(c)). For large values of E_f the one-photon transitions are suppressed due to the Pauli blocking at low energies, and the two-photon response becomes dominant.

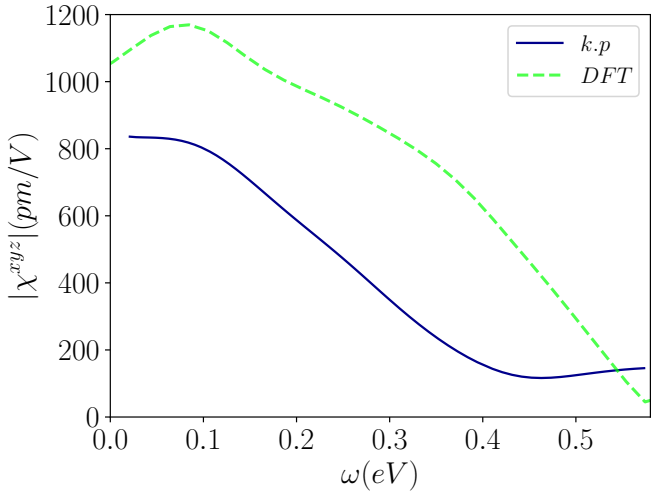

Figure S4. Comparison between χ^{xyz} obtained within the $k \cdot p$ model (blue line) at $E_f = -0.27$ eV and DFT calculations (dashed green line) at $E_f = -0.14$ eV. Both curves are calculated with $\Delta = 0$ eV and $\delta = 0.1$ eV.

E. COMPARING LOW-ENERGY SECOND-HARMONIC GENERATION USING FIRST PRINCIPLES AND $k \cdot p$ CALCULATIONS

To benchmark our DFT calculation we compare this calculation to our results obtained using the low-energy model around the Γ point, described in Sec. . Fig. S4 shows the nonlinear susceptibility of RhSi obtained for $E_f = -0.14$ eV using DFT and $E_f = -0.27$ eV using the $k \cdot p$ results, both computed without many-body effects, i.e., $\Delta = 0$ eV.

Fig. S4 shows that the second-harmonic generation obtained from DFT and the $k \cdot p$ calculations are similar. The broader peak in DFT compared to that of the $k \cdot p$

model can be attributed to extra electronic transitions in DFT, which are not captured by the $k \cdot p$ model. As seen in Fig. S1, the scissors correction suppresses this peak and leads to a better description of the experimental SHG data in RhSi (Fig. 1).

F. LOW-ENERGY SINGLE-PARTICLE SECOND-HARMONIC GENERATION IN TWO-LINEAR-BAND WEYL SYSTEMS: $k \cdot p$ MODEL

Here, we present SHG response for a Weyl system with linear bands close to one of its nodes. We start by the linear Hamiltonian

$$\mathcal{H} = v_{\rm f} \boldsymbol{\sigma}.\boldsymbol{k} = \boldsymbol{h}.\boldsymbol{\sigma}, \tag{F30}$$

, where $v_{\rm f}$ is the Fermi velocity, $\boldsymbol{\sigma} = (\sigma^1, \sigma^2, \sigma^3)$ denote Pauli matrices and $\boldsymbol{k} = (k_x, k_y, k_z)$ stand for the momentum. $\boldsymbol{h} = (h_x, h_y, h_z)$, with $h_i = v_{\rm f} k_i$, $\forall i \in \{x, y, z\}$, are obtained by $SU(2)$ decomposition of $\mathcal{H}$. The eigensystem of the Hamiltonian includes two eigenvalues $\varepsilon_{1,2} = \pm v_{\rm f} k$, associated with eigenvectors $|\psi_{1,2}\rangle = \left(\frac{k_z \mp \sqrt{k_x^2+k_y^2+k_z^2}}{k_x + i k_y}, 1\right)^T$.

To analytically evaluate Eq. (5), we first express Δ^a_{nm} and $r_{nm} = -\imath v_{nm}/\omega_{nm}$ in terms of $\boldsymbol{h}$ as

$$\hbar\omega_{nm} = \varepsilon_n - \varepsilon_m, \tag{F31}$$

$$v^a_{nm} = \langle n|\partial_{k_a} H|m\rangle = (\partial_{k_a} h_\beta)\sigma^\beta_{nm} = h_{\beta,a}\sigma^\beta_{nm}, \tag{F32}$$

$$\Delta^a_{nm} = v^a_{nn} - v^a_{mm} = h_{\beta,a}\left[\sigma^\beta_{nn} - \sigma^\beta_{mm}\right], \tag{F33}$$

where $m, n = \{1, 2\}$ are band indices. Here Pauli matrices with nonzero h in the eigenspace of $\mathcal{H}$, with matrix V, yield

$$V^{-1}\sigma^1 V = \begin{pmatrix} -\frac{k_x}{\sqrt{k_x^2+k_y^2+k_z^2}} & \frac{k_z\left(\sqrt{k_x^2+k_y^2+k_z^2}+k_z\right)-ik_xk_y+k_y^2}{(k_x+ik_y)\sqrt{k_x^2+k_y^2+k_z^2}} \\ \frac{k_z\left(\sqrt{k_x^2+k_y^2+k_z^2}-k_z\right)+ik_xk_y-k_y^2}{(k_x+ik_y)\sqrt{k_x^2+k_y^2+k_z^2}} & \frac{k_x}{\sqrt{k_x^2+k_y^2+k_z^2}} \end{pmatrix}, \tag{F34}$$

$$V^{-1}\sigma^2 V = \begin{pmatrix} -\frac{k_y}{\sqrt{k_x^2+k_y^2+k_z^2}} & \frac{i\left(k_z\left(\sqrt{k_x^2+k_y^2+k_z^2}+k_z\right)+k_x^2+ik_xk_y\right)}{(k_x+ik_y)\sqrt{k_x^2+k_y^2+k_z^2}} \\ \frac{ik_z\left(\sqrt{k_x^2+k_y^2+k_z^2}-k_z\right)-ik_x^2+k_xk_y}{(k_x+ik_y)\sqrt{k_x^2+k_y^2+k_z^2}} & \frac{k_y}{\sqrt{k_x^2+k_y^2+k_z^2}} \end{pmatrix}, \tag{F35}$$

$$V^{-1}\sigma^3 V = \begin{pmatrix} -\frac{k_z}{\sqrt{k_x^2+k_y^2+k_z^2}} & -\frac{k_z}{\sqrt{k_x^2+k_y^2+k_z^2}} - 1 \\ \frac{k_z}{\sqrt{k_x^2+k_y^2+k_z^2}} - 1 & \frac{k_z}{\sqrt{k_x^2+k_y^2+k_z^2}} \end{pmatrix}. \tag{F36}$$

Using commutation and anti-commutation relations of Pauli matrices, we then can rewrite various terms in Eq. (5) as

$$r^a_{nm}\{r^b_{ml} r^c_{ln}\} = \frac{v^a_{nm}\{v^b_{ml} v^c_{ln}\}}{-\imath\omega_{nm}\omega_{ml}\omega_{ln}} = h_{\alpha,a}h_{\beta,b}h_{\gamma,c}\frac{\sigma^\alpha_{nm}\{\sigma^\beta_{ml}\sigma^\gamma_{ln}\}}{-\imath\omega_{nm}\omega_{ml}\omega_{ln}}, \tag{F37}$$

$$r^a_{nm}\{\Delta^b_{ml} r^c_{ln}\} = \frac{v^a_{nm}\{\Delta^b_{mn} v^c_{mn}\}}{\omega^2_{nm}} = h_{\alpha,a}h_{\beta,b}h_{\gamma,c}\frac{\sigma^a_{nm}\{(\sigma^\beta_{mm} - \sigma^\beta_{nn})\sigma^c_{mn}\}}{\omega^2_{nm}}. \tag{F38}$$

Substituting $\boldsymbol{h}$ and matrix elements of Pauli matrices, given in Eqs. (34, 35, 36), into various terms in Eq. (5) and performing momentum-integration results in $\chi^{xyz}(2\omega;\omega,\omega) = 0$.

[1] Baozhu Lu, Jason D Tran, and Darius H Torchinsky, "Fast reflective optic-based rotational anisotropy nonlinear harmonic generation spectrometer," Review of Scientific Instruments **90**, 053102 (2019).

[2] Dylan Rees, Kaustuv Manna, Baozhu Lu, Takahiro Morimoto, Horst Borrmann, Claudia Felser, JE Moore, Darius H Torchinsky, and J Orenstein, "Helicity-dependent photocurrents in the chiral Weyl semimetal RhSi," Science advances **6**, eaba0509 (2020).

[3] Shreyas Patankar, Liang Wu, Baozhu Lu, Manita Rai, Jason D. Tran, T. Morimoto, Daniel E. Parker, Adolfo G. Grushin, N. L. Nair, J. G. Analytis, J. E. Moore, J. Orenstein, and D. H. Torchinsky, "Resonance-enhanced optical nonlinearity in the Weyl semimetal TaAs," Phys. Rev. B **98**, 165113 (2018).

[4] James L. P. Hughes and J. E. Sipe, "Calculation of second-order optical response in semiconductors," Phys. Rev. B **53**, 10751–10763 (1996).

[5] F. Nastos, B. Olejnik, K. Schwarz, and J. E. Sipe, "Scissors implementation within length-gauge formulations of the frequency-dependent nonlinear optical response of semiconductors," Phys. Rev. B **72**, 045223 (2005).

[6] C. S. Wang and B. M. Klein, "First-principles electronic structure of Si, Ge, GaP, GaAs, ZnS, and ZnSe. II. optical properties," Phys. Rev. B **24**, 3417–3429 (1981).

[7] S. Bergfeld and W. Daum, "Second-harmonic generation in GaAs: Experiment versus theoretical predictions of $\chi^{(2)}_{xyz}$," Phys. Rev. Lett. **90**, 036801 (2003).

[8] Yang Chi, Huai-Guo Xue, and Sheng-Ping Guo, "Designing sulfide borate as a novel type of second-order nonlinear-optical material," Inorg. Chem. **59** (2020), 10.1021/acs.inorgchem.9b03426.

[9] Mark S. Hybertsen and Steven G. Louie, "First-principles theory of quasiparticles: Calculation of band gaps in semiconductors and insulators," Phys. Rev. Lett. **55**, 1418–1421 (1985).

[10] F Aryasetiawan and O Gunnarsson, "TheGWmethod," Reports on Progress in Physics **61**, 237–312 (1998).

[11] Hong Jiang, Ricardo I. Gómez-Abal, Xin-Zheng Li, Christian Meisenbichler, Claudia Ambrosch-Draxl, and Matthias Scheffler, "Fhi-gap: A GW code based on the all-electron augmented plane wave method," Computer Physics Communications **184**, 348 – 366 (2013).

[12] Zachary H. Levine and Douglas C. Allan, "Linear optical response in silicon and germanium including self-energy effects," Phys. Rev. Lett. **63**, 1719–1722 (1989).

[13] Banasree Sadhukhan, Yang Zhang, Rajyavardhan Ray, and Jeroen van den Brink, "First-principles calculation of shift current in chalcopyrite semiconductor $ZnSnP_2$," Phys. Rev. Materials **4**, 064602 (2020).

[14] Wenshen Song, Guang-Yu Guo, Su Huang, Lan Yang, and Li Yang, "First-principles studies of second-order nonlinear optical properties of organic-inorganic hybrid halide perovskites," Phys. Rev. Applied **13**, 014052 (2020).

[15] Vyacheslav S. Zhandun and Andrey Nemtsev, "Ab initio study of the magnetic, optical and electronic properties of spinel Co3O4 within DFT and GW approaches," Journal of Magnetism and Magnetic Materials **499**, 166306 (2020).

[16] Zhuoliang Ni, K. Wang, Y. Zhang, O. Pozo, B. Xu, X. Han, K. Manna, J. Paglione, C. Felser, A. G. Grushin, and et al., "Giant topological longitudinal circular photo-galvanic effect in the chiral multifold semimetal CoSi," Nature Communications **12** (2021), 10.1038/s41467-020-20408-5.

[17] Oscar Pozo and Fernando de Juan, "Computing observables without eigenstates: Applications to bloch hamiltonians," Phys. Rev. B **102**, 115138 (2020).

[18] Guoqing Chang, Su-Yang Xu, Benjamin J. Wieder, Daniel S. Sanchez, Shin-Ming Huang, Ilya Belopolski, Tay-Rong Chang, Songtian Zhang, Arun Bansil, Hsin Lin, and M. Zahid Hasan, "Unconventional chiral fermions and large topological Fermi arcs in RhSi," Phys. Rev. Lett. **119**, 206401 (2017).

[19] Felix Flicker, Fernando de Juan, Barry Bradlyn, Takahiro Morimoto, Maia G. Vergniory, and Adolfo G. Grushin, "Chiral optical response of multifold fermions," Phys. Rev. B **98**, 155145 (2018).